Supporting Information

Supplementary Materials and Methods

Animal experiments and slice preparation

All animal experiments were performed in accordance with the guideline of the Japanese Physiological Society and was approved by the animal committee of Doshisha University. Wistar rats of 18–30 days were anesthetized with isoflurane and decapitated, and their brains were dissected. Hippocampal slices (300 μm for patch clamp recording and Ca^{2+} imaging; 150 μm for immunostaining) were prepared acutely from the brains using a linear slicer (VT1200, Leica). The slicing solution contained (in mM): NaCl 87, Sucrose 75, KCl 2.5, $NaHCO_3$ 25, glucose 10, NaH_2PO_4 1.25, $CaCl_2$ 0.5, $MgCl_2$ 7, oxygenated with 95 %O_2 and 5 %CO_2. After slicing, the slices were incubated in the slicing solution for 30 mins at 37℃, and were kept at room temperature afterwards. The electrophysiological experiments were performed within 4 hours after slicing.

Electrophysiology

For slice patch clamp recordings, the slices were transferred to the recording chamber, visualized by an upright microscope (Olympus BX51) and TillVision imaging system (Till Photonics), and perfused with a normal ACSF containing (in mM): NaCl 125, KCl 2.5, glucose 25, $NaHCO_3$ 25, NaH_2PO_4 1.25, ascorbic acid 0.4, myo-inostiol 3, Na-pyruvate 2. $CaCl_2$ 2, $MgCl_2$ 1, oxygenated with 95 %O_2 and 5 %CO_2. For dissociated hMFBs, 10 mM TEACl and 0.001 mM tetrodotoxin (TTX, Wako) were added while NaCl and $CaCl_2$ were changed to 110 and 5 mM, respectively, and a bath solution was

changed every 30 minutes instead of bubbling on the stage. The patch pipette for CA3 pyramidal cells contained (in mM): Cs-gluconate 130, TEACl 20, HEPES 10, MgATP 4, Na_2-phosphocreatine 5, NaGTP 0.5, EGTA 5 (pH 7.3, 320 mOsm). The patch pipette for hMFBs contained (in mM): for hMFBs in slice, Cs-gluconate 130 or CsCl 130, HEPES 20, DM-Nitrophen 2.5, $CaCl_2$ 2, $MgCl_2$ 0.5, NaATP 5, NaGTP 0.5 Fura2FF 0.2 (pH 7.3, 320 mOsm); for dissociated, Cs-gluconate 135, TEACl 20, HEPES 10, Na_2-phosphocreatine 5, MgATP 4, NaGTP 0.3, EGTA 0.5 (pH 7.3, 330 mOsm). CsOH was used for adjustment of pH. For TIRF Ca^{2+} imaging, EGTA was raised to 5 mM, and Oregon green BAPTA 6F (OGB6F, 0.2 mM, Invitrogen) was added. Presynaptic recordings were started at least 2 minutes after electrical access to inside of the cell was achieved. Patch clamp recordings were applied to hMFBs and CA3 pyramidal cells using EPC10/2 amplifier (HEKA). The patch pipettes had a resistance of 10–20 MΩ (hMFBs) 2–5 MΩ (CA3). The series resistance was 10–50 MΩ (dissociated hMFBs), 20–70 MΩ (hMFBs) and 5–15 MΩ (CA3). Series resistance compensation was used so that the residual postsynaptic series resistance was below 5 MΩ. Membrane potential was set to −80–−60 mV, and not corrected for liquid junction potential. Membrane currents were low-pass filtered at 2.9 kHz and sampled at 20 kHz or 50 kHz. Recordings were performed at room temperature (~25℃).

Flash photolysis was applied by UV flash lamp (Rapp), and the $[Ca^{2+}]_i$ was measured by Till imaging system (Polychrome 5, Till Photonics) by excitation wavelengths of 350 and 380 nm (25). Calibration of Fura2FF was performed in vitro. TTX (1 μM) and D-AP5 (50 μM) were present during the recordings. In some experiments involving EPSC recordings, CTZ (100 μM) and UBP310 (5 μM) were present to block desensitization of AMPA receptors and kainate receptors, respectively

(Figs. 1, 2 and SI Appendix, Fig. S1). For presynaptic capacitance measurement, sinusoidal voltage stimulations (30 mV in amplitudes, 1000 Hz) were applied to the presynaptic terminal and capacitance was measured using the lock-in software in the Patchmaster Program (HEKA). In Fig. 5 and SI Appendix, Fig. S4 and S5, the capacitance after the depolarization was measured as the average over 50 ms at the plateau phase of the capacitance that appeared after the inward current, because the tail current causes the phase shift and biases the capacitance trace. The capacitance traces at the tail currents were truncated in Fig. 5*B* and *C* and SI appendix, Fig. S4*B* and S5*A*. For some terminals, the capacitance in response to 2-ms pulse was recorded three times and averaged before analysis in order to reduce the noise. As the ΔC_ms were not significantly different from those measured at the non-averaged single traces, the data were pooled and analyzed together.

For extracellular stimulation of mossy fibers, a glass pipette (with a similar size as the patch pipette) contacting a normal ACSF was positioned at the mossy fiber region, similar to ref. 32. We consider the response from a single hMFB when the EPSCs show all-or-none responses when the stimulation intensity was gradually increased. For the experiments testing Ca^{2+} channel blockers, we have not used a minimal stimulation method as described above, in order to get stable responses. The same stimulation intensity has been used throughout the experiment. In some recordings (n = 5), 1 μM DCG-IV, an agonist of group II metabotropic glutamate receptors, was applied in order to confirm the MF-CA3 responses (Supplementary ref. 1), and diminished the EPSCs to ~20 (19 ± 5) %, indicating that we mainly stimulated mossy fibers. In addition, repetitive stimulation facilitated EPSCs, which is a typical feature of MF-CA3 synapses.

For pharmacological experiments, drugs were applied intracellularly (via a patch electrode) or extracellularly (via a bath or a puff solution). The puff electrode filled with the solution had a resistance < 3 MΩ and was subjected to a pressure by a manual syringe. cAMP/PKA signaling was activated by intracellular 0.5 mM cAMP (TCI) or extracellular 50–100 μM forskolin (Abcam). ω-agatoxin IVA (0.2–1 μM, Peptide) and ω-conotoxin GVIA (0.2–1 μM, Peptide) were added extracellularly to block the P/Q- and N-type Ca^{2+} channels, respectively. KT5720 (1 μM, Tocris) was added to the extracellular solution in order to block a PKA activity. An effect of a drug was assessed ≥ 2 minutes after the application.

Dissociation of hMFBs and Ca^{2+} imaging

The procedures were similar to those described in the previous studies (24). Dentate gyrus and CA3 regions were clipped out from the acute hippocampal slices and exposed to an ACSF containing 0.5–5 mg/ml papain (Wako, ≥ 0.5 units/g) activated by 5 mM cysteine for 10–15 minutes at 37℃ before rinsed with a ACSF containing 0.1 mg/ml BSA to suppress the reaction. The regions were then triturated mechanically with a Pasteur pipette and suspended in an ACSF with 0.4 mg/ml DNase (Worthington). Drops of the suspension were plated on a glass bottom dish (D111300, Matsunami Glass) coated with 0.1–0.2 mg/ml concanavalin A (Wako). The dissociated preparation was then incubated for 30 minutes in an ACSF containing 0.001 mM TTX at room temperature, allowing the hMFBs to adhere to the glass.

For measurements, the dish was transferred on the stage of an inverted microscope (Nikon eclipse Ti-u) equipped with a custom-made TIRF system: a 488-nm laser (OBIS488, Coherent) was applied at 2.8–3.6 mW through an optical path

(Sigmakoki) and an oil-immersion 100× objective lens (Apo TIRF100XC, NA = 1.49, Nikon). A dissociated hMFB was identified as a round-shape structure showing inward Ca^{2+} current and a cell capacitance below 10 pF under whole-cell patch clamp condition. A focal plane was set at the footprint of the hMFB visualized by the excitation light. Emission was cut out by a long-pass filter (520 nm) and detected by an sCMOS camera (Zyra5.5 sCMOS, Andor). The operations of the laser and the camera were synchronized with a pulse protocol via a stimulator (Master 8, A. N. P. I, or Electronic Stimulator, Nihon Kohden). Images were taken at 200 Hz with an exposure time of 2.5 ms in image acquisition software (SOLIS, Andor).

Deconvolution analysis of EPSCs

Transmitter release rates were estimated by the deconvolution method (29). The EPSCs were deconvolved with the mEPSC waveform to estimate the release rates, assuming no residual currents due to delayed clearance of neurotransmitter. A previous study indicated that the cumulative release estimated from the deconvolution method match relatively well with the amplitudes of capacitance jumps, suggesting that the EPSCs are a linear summation of mEPSCs (24). In order to fit the relationship between $[Ca^{2+}]_i$ and release and the local Ca^{2+} concentration at the release site during an action potential, we used the transmitter release model, which is the same as the one introduced by ref. 25. Ca^{2+} is bound to 5 Ca^{2+} binding sites sequentially followed by a Ca^{2+}-insensitive step before a synaptic vesicle fuses. The following parameters were used: $k_{on} = 1.2 \times 10^8\ M^{-1}s^{-1}$, $k_{off} = 10000\ s^{-1}$, $b = 0.25$; $\gamma = 6000\ s^{-1}$. The values were similar to ref. 25 as well as ref. 26.

TIRF analysis

The acquired images were analyzed with ImageJ Fiji (NIH), and values were further processed with calculation software (Excel, Microsoft; Igor, Wavemetrics). For Ca^{2+} imaging, background intensity was subtracted from the raw images. To detect a peak of a Ca^{2+} spot from a region of interest, “Find Maxima” plugin was used and specified the position of the largest increase of fluorescence upon the depolarization. F/F_0 was calculated as the fluorescence over the average fluorescence before depolarization, and the mean F/F_0s inside the most inner circle (Fig. 4*F*, light green; “midmost”, r = 0.26 μm) and at the filled areas between the adjacent circles (“annuli”) were measured for radii of 0.39, 0.52, 0.65, 0.78 and 0.91 μm, from inner to outer, respectively (Fig. 4*F*). A Ca^{2+} spot was defined as a region, which showed 20 % increases of F/F_0 in the midmost accompanied with gradual decreases of F/F_0 toward the peripheral regions in the two consecutive frames (5 and 10 ms after the stimulus onset). The regions were cropped so that the peak location was centered (Fig. 4*D–F* and SI appendix, Fig. S3*A*). In some F/F_0 image sequences, background noise was quenched by removal of low intensity pixels (e.g. below 1 percentile) before calculation of F/F_0 for clear display of the Ca^{2+} spot. The intensity for a whole bouton was measured at the region inside the edge of the footprint (Fig. 4*K* and SI appendix, Fig. S3*F*).

Immunostainings

150-μm hippocampal slices were pre-incubated in control ACSF or ACSF containing forskolin (50 μM) for 10 minutes at room temperature before fixation in 0.1 M phosphate buffer (PB) solution with 4 % paraformaldehyde (pH = 7.4, Wako) for 1 hour at RT. The slices were preserved in a 0.1 M PB solution (pH = 7.4) with 0.03 % NaN_3

until use. One slice was sampled for one condition from one animal, and samples were stained with equal conditions.

For immunostaining, the fixed slices were permeabilized for 2 hours and 30 min and treated in 0.1 M PB solution (pH = 7.4) with 0.3 % Triton X-100 except for the final washing process. The slices were blocked with 5 % normal goat serum for 1 hour at room temperature and exposed to primary antibodies diluted in 0.1 M PB solution (pH = 7.4) with 0.3 % Triton X-100 for 2 days at 4℃: guinea pig anti-Cav2.1 (1:500); rabbit anti-Munc13-1 (1:150); chicken anti-Homer1 (1:200); mouse anti-Zinc transporter 3 (ZnT3; 1:500); all purchased from Synaptic systems (Germany). After washing every 15 min for 3 hours, the secondary antibodies were applied for 2 hours at RT: Goat anti-rabbit STAR RED (Abberior, Germany; 1:100 or 1:300); Goat anti-guinea pig Alexa Fluor 594 (Invitrogen, Germany; 1:100); Goat anti-chicken Alexa Fluor 488 (Invitrogen, Germany; 1:100 or 1:300); Goat anti-mouse ATTO490LS (Hypermol, Germany; 1:100). The slices were washed with 0.1 M PB buffer (pH = 7.4), mounted with ProLong Gold (Thermo Fisher Scientific) and coverslipped on the slides with high precision coverslips (1.5 H, Roth, Germany).

Time gated STED microscopy and image analyses

Time gated STED (gSTED) microscopy was performed using an Abberior Instruments Expert Line STED setup equipped with an inverted IX83 microscope (Olympus, Japan), two pulsed STED lasers for depletion at 775 nm (0.98 ns pulse duration, up to 80 MHz repetition rate) and at 595 nm (0.52 ns pulse duration, 40 MHz repetition rate) and pulsed excitation lasers (at 488 nm, 561 nm and 640 nm). Mossy fibers were identified by ZnT3 labeling and imaged in the CA3 stratum lucidum close to CA3 pyramidal cell

bodies, where hMFBs make contact on proximal dendritic spines of CA3 pyramidal neurons (Supplementary ref. 2). Confocal and multi-channel gSTED scanning was performed with 100× oil-immersion objective lens (Olympus, NA = 1.4). The dyes STAR RED and Alexa Fluor 594 were depleted with a pulsed STED laser at 775 nm. Alexa Fluor 488 was depleted with a pulsed STED laser at 595 nm. Time gating was set at 750 ps. Fluorescence signals were detected sequentially by line by avalanche photodiode detectors at appropriate spectral regions. Alexa Fluor 488 confocal and gSTED images were acquired following acquisition of the other channels. ATTO490LS was excited at 488 nm and detected between 650–765 nm in conventional confocal mode. 2D gSTED and confocal images were acquired with a pixel dwell time of 2 µs, with 30x lines accumulation and 10x line accumulation, respectively, at 16-bit sampling and a field of view of 10 µm x 10 µm. Lateral pixel size was set to 20 nm. Experiments were repeated two times on different biological replicates and 5–14 images were acquired from one slice per animal. These procedures were operated by computer software (Imspector, version 16.1.6477, Abberior Instruments, Germany).

Raw triple-channel gSTED images were processed for Richardson-Lucy deconvolution using the Imspector software (version 16.1.6477, Abberior Instruments, Germany). The point spread function was automatically computed with a 2D Lorentz function having a full- width half- maximum of 40 nm, based on measurements with 40 nm Crimson beads. Default deconvolution settings were applied.

For all gSTED analyses, analyses were done in a blind manner. Files belonging to a given rat hippocampal slice were labeled with a unique number, analyses were performed on the corresponding files labeled with slice numbers and then reassigned to the corresponding group. gSTED analysis to determine Cav2.1

density and average area was carried out based on a ZnT3-positive confocal mask to select Cav2.1 clusters on deconvolved gSTED images. Cav2.1 clusters in the ZnT3-positive area (SI Appendix, Fig. S7) were selected using the ImageJ Image Calculator plugin (operation: min), upon Gaussian blur (Sigma-radius: 2) and thresholding of the raw ZnT3 confocal images. To measure the area and number of Cav2.1 clusters per ZnT3-positive area, the resulting 8-bit deconvolved Cav2.1 images were thresholded, then Cav2.1 signals were segmented with the function Find Maxima and quantified with the Analyze Particles plugin (ImageJ). Particles smaller than 2 pixels (below the resolution achieved) were not considered. Thresholds and segmentation parameters were kept constant within the same experiment.

For peak-to-peak line profile measurements, well-defined side view or planar synapses, having Cav2.1 and Munc13-1 spots on the same focal plane, were identified and manually sampled based on their orientation relative to Homer1 clusters, without direct use of a ZnT3-positive confocal mask. Here, synapses were sampled and considered belonging to hMFBs when located within areas with high density of active zones, corresponding to the distribution of the ZnT3 signal and thereby to hMFBs (see Fig S7A, showing Cav2.1 signal enriched in ZnT3-positive areas), as previously published (43). The co-labeling with Homer1 allowed us to determine Cav2.1 and Munc13-1 cluster orientation relative to a given PSD, thereby indicating presynaptic clusters belonging to a single active zone, and to exclude inhibitory synapses that might be present in the CA3 stratum lucidum (ref. 43 and Supplementary ref. 3). Presynaptic Cav2.1 and Munc13-1 clusters were then identified as a pair opposed in close proximity to Homer1 signals and approximately 8 synapses per image were sampled on deconvolved 8-bit gSTED images. Line profile measurements of distances

between spots (Fig. 6*B*–*D*) were performed in ImageJ (version 1.52i, NIH). According to the parameters described above, synapses were manually traced with the line profile tool (thickness 1 pixel/20 nm) and peak intensities across the line were retrieved for the Cav2.1 and the Munc13-1 channel using the ImageJ Macro ("Macro_plot_lineprofile_multicolor" from Kees Straatman, University of Leicester, Leicester, UK). Intensity values from individual synapses were exported to Excel. Local maxima were calculated with the SciPy "argrelmax" function, as described in ref. 43, in order to obtain peak intensities for different image channels and peak-to-peak distances. Values were then averaged per animal.

The locations of the presynaptic Cav2.1 clusters within 200 nm radius from Munc13-1 clusters (SI Appendix, Fig. S9) were determined on 8-bit deconvolved images by their peak locations detected with the Find Maxima plugin (ImageJ), or as center of the clusters, without direct use of a ZnT3-positive confocal mask. Cav2.1 clusters were defined as belonging to a given active zone when located within a 200 nm radius from a Munc13-1 cluster, previously identified by line profile measurements. The 200 nm radius was set based on previous findings regarding mossy fiber active zone size (10 and 44). The number of Cav2.1 clusters and distances between closest Cav2.1 neighbor and Munc13-1 clusters within this 200 nm radius were measured with a custom-made ImageJ macro.

The sizes of presynaptic closest Cav2.1 or Munc13-1 clusters were measured on 16-bit raw STED images (Fig. 7 and SI Appendix, Fig. S10) by line profiles centering a given peak, normalized to the intensity at the peak of the target cluster and fitted to Gaussian function in Igor Pro software:

$$\mathrm{y} = y_0 + \mathrm{A} * \exp(-\mathrm{x}/\sigma)^2$$

where y_0 is basal intensity, A is peak intensity from the base, and σ is standard deviation. The average values of these parameters for Cav2.1 were (y_0, A, σ): 0.44, 0.43, 59.6 nm in control and 0.44, 0.40, 68.4 nm in forskolin; for Munc13-1 0.56, 0.33, 84.3 nm in control and 0.56, 0.34, 83.9 nm in forskolin. Full width of half-maximum amplitudes (FWHM) were yielded as $2 * \sqrt{\ln 2} * \sigma$. The similarites in y_0 between control and forskolin treated samples validate the reliability of the Gaussian fits and therefore of the comparisons of FWHMs for both Cav2.1 and Munc13-1. For classification of the Cav clusters in relation to the distances from the Munc13-1 cluster (Fig. 7*G*–*I*), the distances measured in SI Appendix, Fig. S9 were used. For 2D Gaussian fitting on averaged images (Fig. 7*I*), the ImageJ macro “2D Gaussian” written by Dominic Waithe was used.

Statistics

Statistical analyses were performed in Prism (version 7.03, GraphPad, La Jolla, CA, USA), Excel or Igor Pro (mainly version 7.0.6.1). Values are shown as average ± standard error of mean in the text and figures. In some graphs in the figures, the data points from the same cell (Fig. 3) or animal (Figs. 6, 7 and SI Appendix, Figs. S7–10) were connected with a line. Normality was assessed with the Shapiro-Wilk test and inspecting data distribution. For significance test, paired or unpaired t-test was performed to compare two groups, unless otherwise stated. Difference in variance was tested with f-test before paired or unpaired t-test. Only two-tailed p values were considered.

Supplementary Figure 1

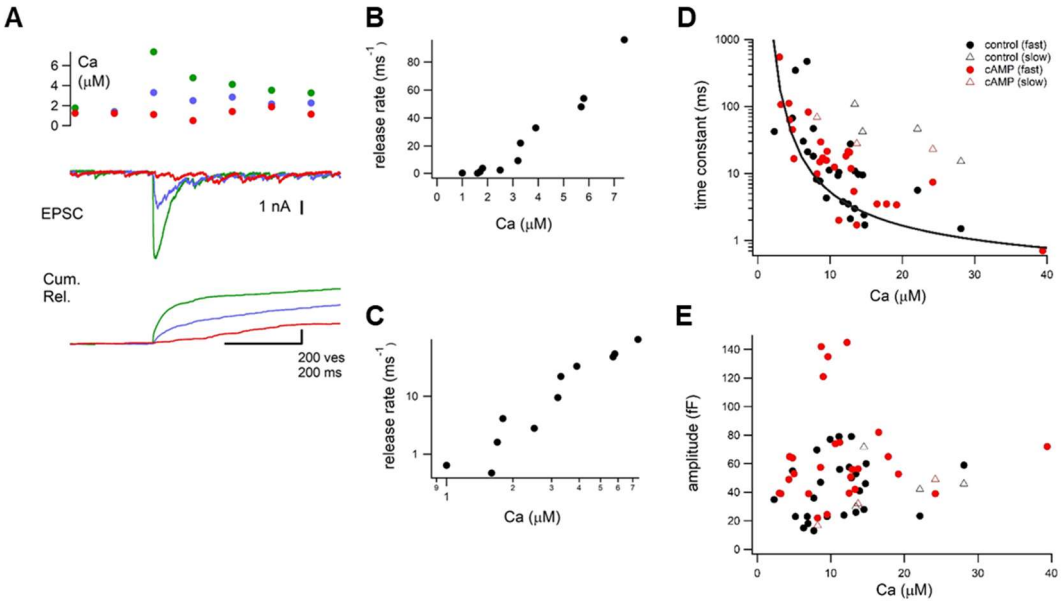

Supplementary Fig. 1. The intracellular Ca^{2+} dependence of transmitter release and the amplitudes of the fast and slow components of capacitance jumps.

(*A*) The example traces from a single cell pair showing the intracellular Ca^{2+} dependence of transmitter release. From top, the intracellular Ca^{2+} concentration, EPSCs and cumulative release are shown. Different colors show the different trials from the same cell pair. (*B* and *C*) The intracellular Ca^{2+} dependence of the peak release rate per vesicle in the linear (*B*) and the log-plot (*C*), respectively. (*D*) The relationship between the release time constants measured by capacitance measurements (estimated from exponential fitting) and the Ca^{2+} concentration. In *D* and *E*, black and red dots show the individual data of the fast release from control condition and in the presence of cAMP, respectively. In some cases, the slow component of release existed and dual exponential fits were used (open triangles). (*E*) The amplitudes of fast and slow release measured by capacitance measurements. The fast component displayed a capacitance jump of ~50 fF (45.6 ± 6.1 fF and 59.6 ± 7.1 fF in control and cAMP conditions, n = 10 and 7 cells, $P > 0.05$). The slow component had a capacitance jump of 47.4 fF and 32.6 ± 9.3 fF in control and cAMP conditions, respectively (n = 1 and 3 cells).

Supplementary Figure 2

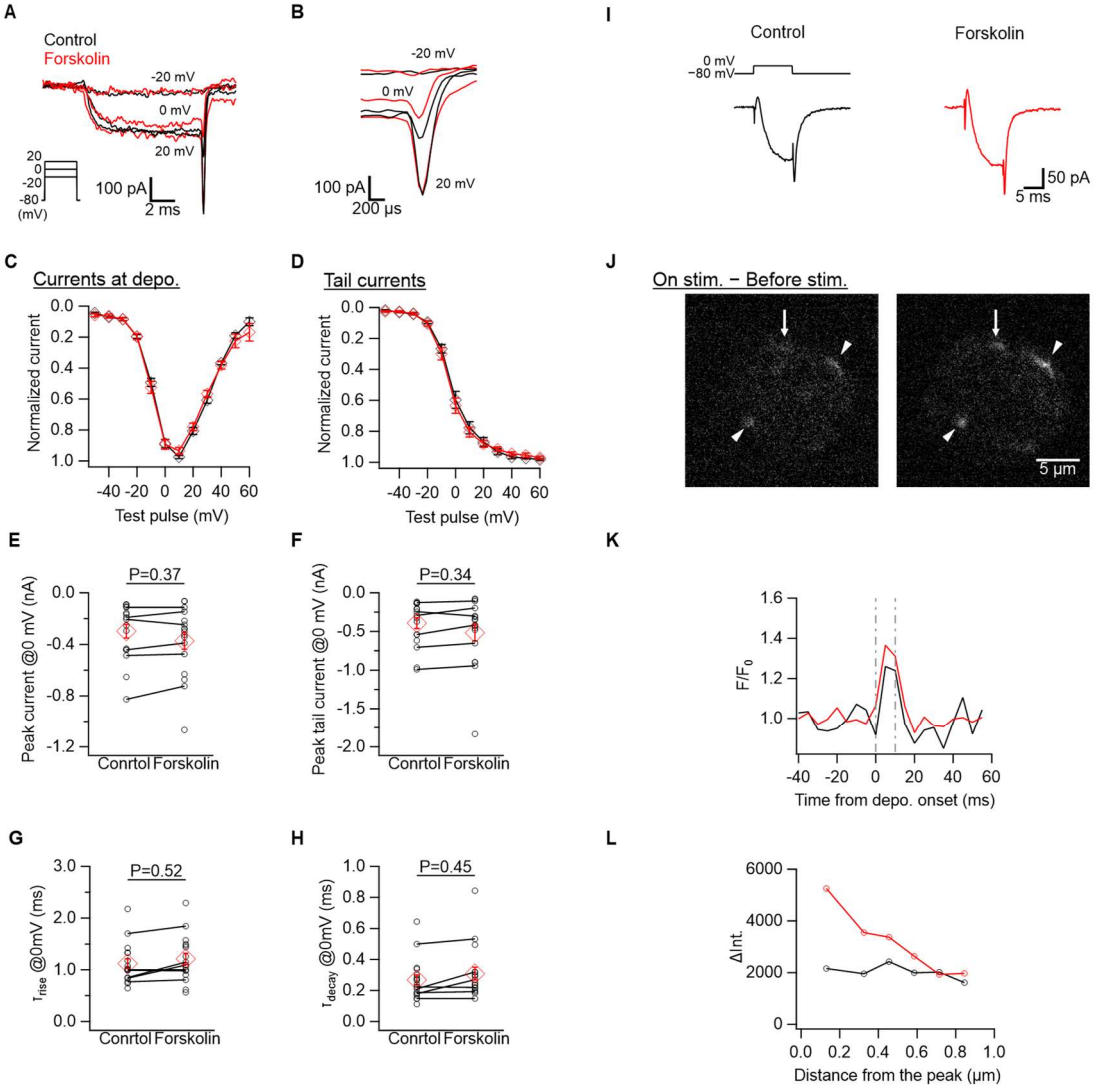

Supplementary Fig. 2. Ca^{2+} currents and local Ca^{2+} influx before and after forskolin application.

(*A*) Ca^{2+} currents were induced by 10-ms depolarization to -20, 0 and 20 mV before (control, black) and after 50 µM forskolin application (red) in the dissociated hMFB. Leak currents were subtracted. (*B*) Magnified view of the tail currents in *A*. (*C* and *D*) I-V relationships without (black) and with forskolin (red) for currents at the test pulses (-50–60 mV, a 10-mV step; *C*) and for their tail currents (*D*). Ca^{2+} current amplitudes of each bouton were normalized by the maximum value. In *D*, fitting the curves to Boltzmann equation estimates V_{half}s and slope factors at -1.7 and 9.4 mV for control conditions, and -3.0 and 9.3 mV for the forskolin conditions, respectively. In *C–H*, data were obtained from 12 terminals in both control and forskolin conditions. (*E* and *F*)

Peak amplitudes of the Ca^{2+} current at 0-mV test pulse (*E*) and at its tail current (*F*) without (control) and with forskolin. In E–H, data acquired from the same terminals were connected with the lines (n = 6). (*G* and *H*) Time constants of activation of the Ca^{2+} current at the 0-mV test pulse (*G*) and of decay of its tail current (*H*) without (control) and with forskolin. (*I* and *J*) Ca^{2+} current induced by the depolarization (0 mV, 10 ms; *I*) and differences of OGB6F fluorescence between before and during the depolarization in *I* (*J*), before (control, left) and after the application of forskolin (50 μM) (right). Arrowheads in *J* indicate the spots where the fluorescence intensity locally increased in response to depolarization. Note that the local Ca^{2+} influx was increased after forskolin application (arrows in *J*). The amplitudes of the local Ca^{2+} transients were increased after forskolin application in 5 out of 8 terminals. (*K*) F/F_0s were calculated for the spots indicated by the arrows in *J*. In *K* and *L*, before (black) and after forskolin application (red). (*L*) Mean intensities at the midmost and annuli of the local sites indicated by the arrows in *J* are plotted against the distance from the spot center at 5 ms after the onset of depolarization.

Supplementary Figure 3

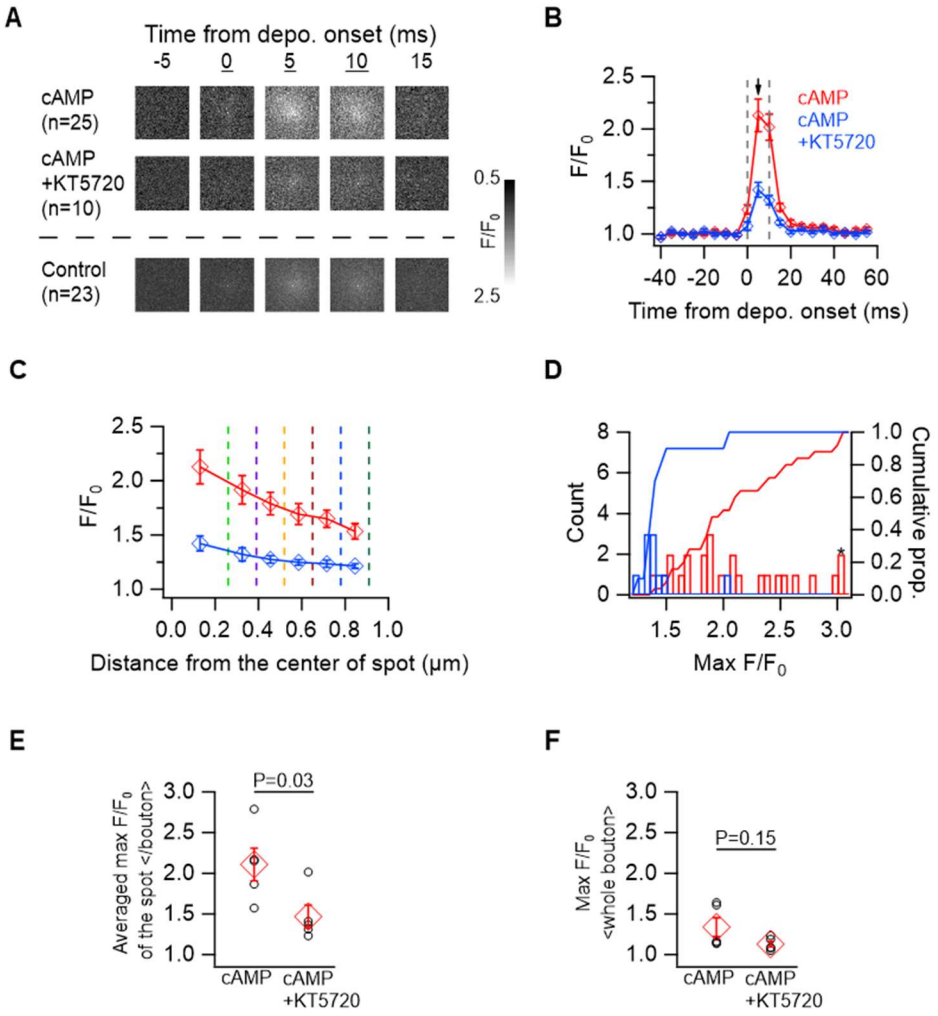

Supplementary Fig. 3. A PKA blocker diminishes the cAMP-dependent increase in local Ca^{2+} influx.

(*A*) Sequential F/F_0 images of the averaged spots for cAMP (top), cAMP with extracellular 1 μM KT5720, a PKA inhibitor (middle), and control conditions (bottom). Five consecutive frames across the depolarization (from 0 to 10 ms, underlined numbers) were shown. The Ca^{2+} spots were centered in a 2 μm×2 μm cropped square. In *A*–*F*, the data for control and cAMP conditions are the replicates of Fig. 4. In the presence of cAMP with KT5720, the inward current was induced in the same way as Fig. 4*A*; an amplitude of the current is -248.2 ± 73.4 pA, and a number of spots was 2.0 ± 0.6 (n = 5). Note that increase in the local Ca^{2+} influx by cAMP was reduced to the control level in the presence of cAMP and KT5720. (*B*) Sequential F/F_0 changes at the midmost in cAMP and cAMP with KT5720. Gray dashed lines indicate the onset and

the end of depolarization. In *B* and *C*, the values are the averages of 25 and 10 spots from 5 and 5 animals for cAMP and cAMP with KT5720, respectively. In *B*–*D*, cAMP (red) and cAMP with KT5720 (blue). (*C*) F/F_0s are plotted against the distance from the spot center at 5 ms after the onset of depolarization (arrow in *B*) in cAMP and cAMP with KT5720. The vertical dotted lines correspond to the radius of the circles in Fig. 4*F*, and each diamond indicates the mean F/F_0 at the area. (*D*) Histograms and cumulative graphs of maximum F/F_0 at the midmost for cAMP and cAMP with KT5720. The values over 3.0 were pooled at the rightest (asterisk). Statistical significance was evaluated by two samples Kolmogorov-Smirnov test ($P = 4.1\times10^{-5}$). (*E*) Maximum F/F_0 at the midmost were averaged per bouton for cAMP and cAMP with KT5720. (*F*) Maximum F/F_0 in the whole bouton in cAMP and cAMP with KT5720.

Supplementary Figure 4

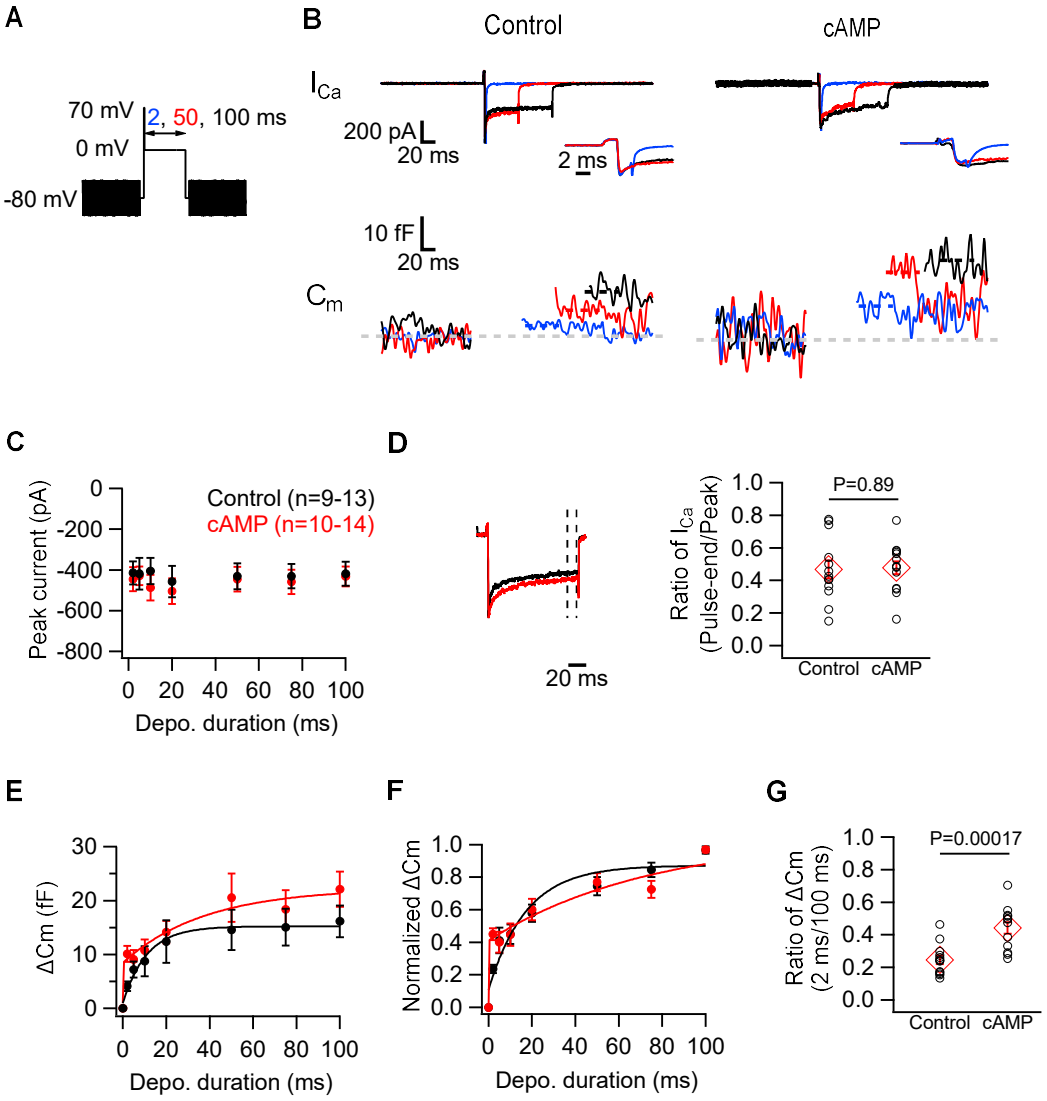

Supplementary Fig. 4. cAMP accelerates SV exocytosis in hMFBs.

(*A*) Same as Fig. 5*A*. Scheme of the pulse. (*B*) Same as Fig. 5*B*. Ca^{2+} current and C_m were measured without (control, left) and with cAMP (0.5 mM) in the patch pipette (right). The depolarization induced Ca^{2+} currents (top) and the membrane capacitance jump (bottom). The examples at the 0-mV depolarization for 2 ms (blue), 50 ms (red) and 100 ms (black) are shown. The traces at the 2-ms pulses are the averages of 3 trials, and the capacitance after the depolarizing pulse was measured at the periods indicated by the dotted lines. Note that increase of the C_m caused by the 2-ms depolarization was prominent with cAMP. (*C*) The peak Ca^{2+} current is plotted against the duration of 0-mV depolarization for control and cAMP. In *C*–*F*, control (black) and

cAMP (red). (*D*) Ca^{2+} current elicited by the 100-ms depolarization normalized by the peak amplitude (left). Representative traces are different from the data set in *B*. The ratio of the amplitude at the end of depolarization to the peak was calculated for control and cAMP, indicating inactivation of Ca^{2+} currents was not modified by cAMP (right). When the decay phase was fitted by a double-exponential function, the fast time constant was 2.7 ± 0.9 ms and 3.3 ± 0.7 ms, while the slow time constant was 31.0 ± 6.6 ms and 36.1 ± 7.5 ms, in control (n = 12) and with cAMP (n = 14), respectively. Both components did not show significant differences (fast, P = 0.55; slow, P = 0.61; unpaired t-test). (*E*) ΔC_m in relation to the duration of 0-mV depolarization for control and cAMP. The solid lines are the results of a single (11.0 ms; for control) and a double exponential fitting (0.083 and 37.8 ms; for cAMP). Although the capacitance jumps were somewhat larger for longer durations (> 50 ms) and this may suggest enhanced synaptic vesicle replenishment, the differences were not statistically significant. (*F*) The ΔC_ms were normalized by the maximum and then plotted in the same way as *E*. (*G*) The ΔC_m by the 2-ms depolarization relative to that by the 100-ms one was evaluated for control and cAMP.

Supplementary Figure 5

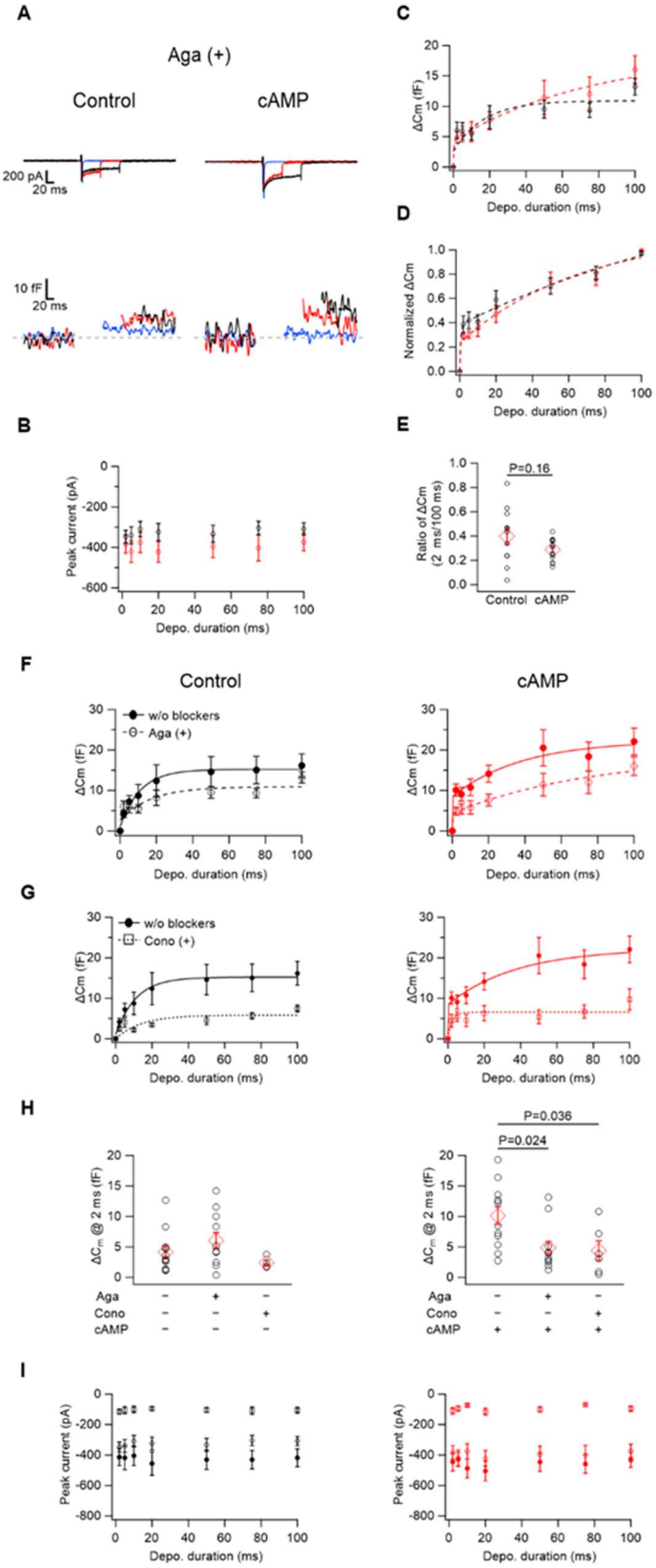

Supplementary Fig. 5. Effects of Ca^{2+} channel blockers on the cAMP-dependent acceleration of exocytosis.

(*A*) Same as Fig. 5*C*. Ca^{2+} current and C_m were measured without (control, left) and with cAMP (0.5 mM) in the patch pipette (right). ω-agatoxin (Aga) was present in the extracellular solution. The depolarization induced Ca^{2+} currents (top) and increased the membrane capacitance (bottom). The examples at the 0-mV depolarization for 2 ms (blue), 50 ms (red) and 100 ms (black) are shown. The traces at the 2-ms pulses are the averages of 3 trials, and the capacitance after the depolarizing pulse was measured at the periods indicated by the dotted lines. (*B*) The peak Ca^{2+} current is plotted against the duration of 0-mV depolarization for control and cAMP. In *B*–*D*, *F*, *G* and *I*, control (black) and cAMP conditions (red) are shown. (*C*) The ΔC_m in relation to the duration of 0-mV depolarization for control and cAMP. In *C* and *D*, dashed lines indicate the results of single or double exponential fitting. (*D*) The ΔC_ms were normalized by the maximum and then plotted in the same way as *C*. (*E*) The ΔC_m by the 2-ms depolarization relative to that by the 100-ms one was evaluated for control and cAMP. (*F* and *G*) ΔC_ms were plotted against the duration of the 0-mV depolarization without (filled circles) and with either Aga (*F*; open circles, same as Fig. 5*D*) or ω-conotoxin GVIA (Cono, 1 μM; *G*; open squares). In *F*–*I*, without (control; left) and with cAMP in the patch pipette (right). Note that Aga suppressed ΔC_m even at the short depolarization particularly in the presence of cAMP. In *F* and *G*, the data for the conditions without Ca^{2+} blockers and with Aga are the same as Fig. 5*D* (*F*). The Cono effect to suppress ΔC_m seemed rather positive almost throughout these pulse durations, irrespective of the presence of cAMP (*G*). The results of a single or a double exponential fitting are following (control vs. with cAMP): 11.0 ms vs. 0.083 and 37.8 ms without Ca^{2+} channel blockers (solid lines); 16.7 ms vs. 0.2 and 75.7 ms with Aga (dashed lines in *F*); 14.0 ms vs.2.2 ms with Cono (dotted lines in *G*). (*H*) ΔC_ms at 2-ms depolarization without the Ca^{2+} channel blockers and with either Aga or Cono. Statistical significances were assessed by Kruskal-Wallis test for control ($P = 0.15$) and cAMP conditions ($P = 0.014$), and P values in the right panel were the results of Dunn's post-hoc multiple comparisons test between control and either Aga or Cono group. (*I*) Amplitudes of the peak Ca^{2+} current plotted against the pulse durations without the Ca^{2+} channel blockers (filled circles) and with either Aga (open circles) or Cono (open squares). Numbers of hMFBs tested for each condition is following (control vs. with cAMP): 9–13 vs. 10–14 without Ca^{2+} channel blockers; 8–15 vs. 8–13 with Aga; 4 vs. 3–6 with Cono.

Supplementary Figure 6

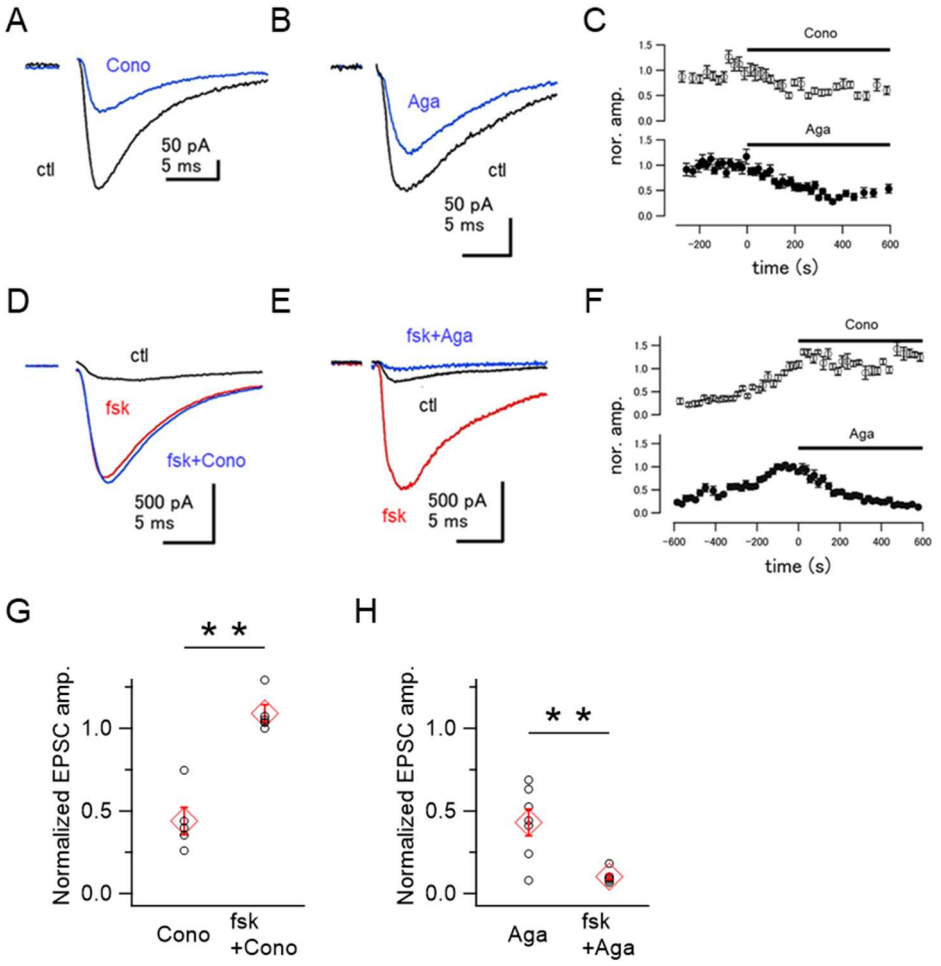

Supplementary Fig. 6. The blocking effect of Aga on the EPSCs greatly increases after the forskolin application.

(*A* and *B*) The mossy fiber-evoked EPSCs were recorded at MF-CA3 synapses before (black; "ctl") and after the application of Ca^{2+} channel blocker (blue in *A*: 0.2 μM Cono; blue in *B:* 0.2 μM Aga). EPSCs were reduced by either Cono (n = 7) or Aga (n = 5) application (black to blue). The data are from different cells. In *A*, *B*, *D* and *E*, the traces are the averages of 5–30 trials, and the stimulus artifacts were concealed. (*C*) The time course of EPSC amplitudes after application of Ca^{2+} channel blockers. In *C*, *F*, *G* and *H*, EPSC amplitudes were normalized by the amplitude before the blocker application starting at 0 s. (*D* and *E*) The same type of the experiments as A and B, but forskolin was applied (red) before the application of Cono (blue in *D*) or Aga (blue in *E*). Forskolin augmented the EPSCs (black to red), and the augmented EPSCs were reduced greatly by Aga (n = 6; *D*), but little by Cono (n = 5; *E*) (red to blue). The data are from different cells. (*F*) The time course of the EPSC amplitudes after application of

Ca^{2+} channel blockers. Before application of the blockers, forskolin was applied. (*G* and *H*) EPSC amplitudes after either Cono (*G*) or Aga application (*H*). The differences between the conditions without and with forskolin are significant for both Cono and Aga (**P < 0.01, unpaired t-test). Note that the blocking effect of Cono after the forskolin application could be underestimated, due to counterbalance between forskolin-induced potentiation and Cono effect.

Supplementary Figure 7

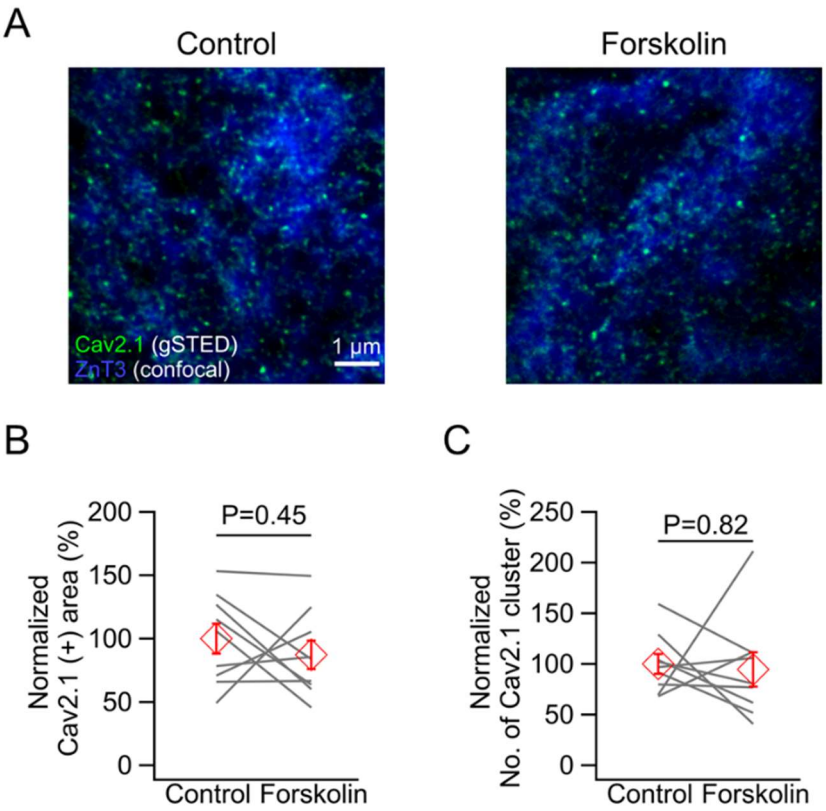

Supplementary Fig. 7. Forskolin application does not significantly alter Cav2.1 cluster density in ZnT3-positive hMFBs.

(*A*) Deconvolved gSTED images of Cav2.1 clusters (green) and raw confocal signals of ZnT3 (blue), a marker for hMFBs, were overlapped in control (left) and forskolin (right) hippocampal slices (150 µm). (*B* and *C*) Areas covered by an average Cav2.1 segmented signal (*B*) and number of Cav2.1 clusters within the ZnT3-positive areas, normalized to control (*C*). The values were averaged per animal, normalized by the mean of the control animals from the same staining condition and compared between control and forskolin within the same animal (n = 9, gray lines).

Supplementary Figure 8

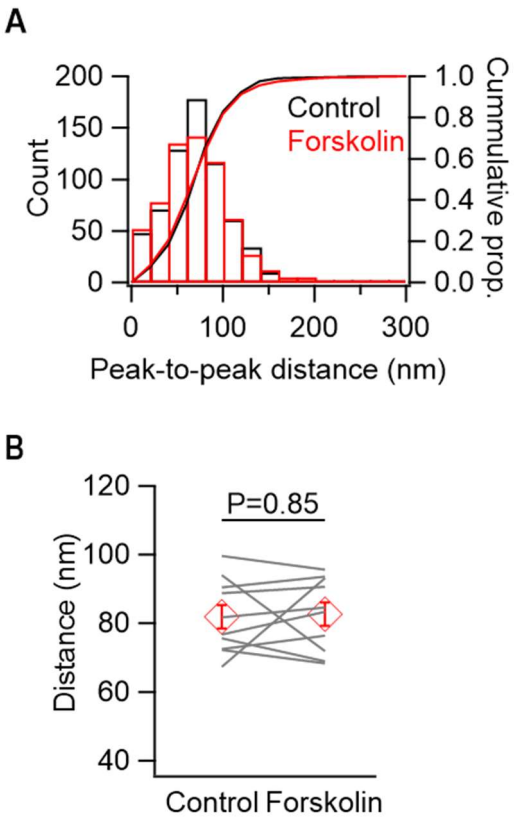

Supplementary Fig. 8. Forskolin application does not significantly alter the mean peak-to-peak distance between Munc13-1 and Cav2.1 clusters at hMFBs.

(*A* and *B*) Histograms and cumulative distributions of the peak-to-peak distances in control (black; n = 653 synapses) and forskolin (red; n = 641 synapses) in a bin of 20 nm (*A*). Peak locations were determined as shown in Fig. 6*B*. The distances were averaged per animal and compared between the conditions (*B*). Data were acquired from 10 animals. For *A*, statistical significance was tested with two samples Kolmogorov-Smirnov test (P = 0.85).

Supplementary Figure 9

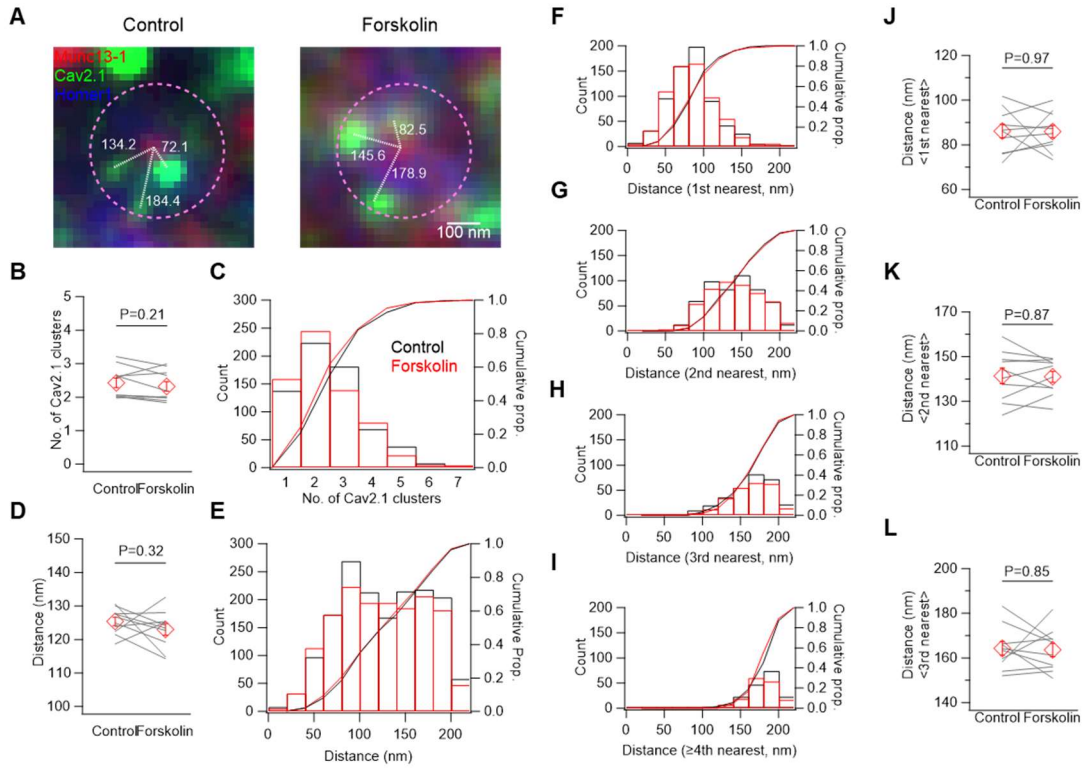

Supplementary Fig. 9. Forskolin application does not significantly alter either the number of Cav2.1 clusters close to release sites or their peak-to-peak coupling distances.

(*A*) Cropped deconvolved gSTED images showing Cav2.1 clusters (green) near a given Munc13-1 cluster (red) adjacent to Homer1 signals (blue) in control (left) and forskolin-treated hippocampal slices (right). The Munc13-1 cluster was centered, and the number of Cav2.1 clusters within 200 nm (pink dashed circles) of the Munc13-1 cluster and their respective distances were quantified. 200 nm radius was based on previous findings regarding mossy fiber active zone size (44). The white dotted lines and numbers indicate the peak-to-peak distances between Munc13-1 and the Cav2.1 clusters (nm). (*B* and *D*) Averages of the number of the Cav2.1 clusters (*B*) and Cav2.1–Munc13-1 distances (*D*). The values averaged per animal were compared between control and forskolin. The data points obtained from the same animal were connected with the gray line. (*C* and *E*) Histograms and cumulative proportions of the number of the Cav2.1 clusters (*C*) and Cav2.1–Munc13-1 distances (*E*). From 10 animals, 660 and 655 Munc13-1 clusters and 1657 and 1558 Cav2.1 clusters were analyzed in control and forskolin conditions, respectively. In *C* and *E*–*L*, in control

(black) and forskolin (red). In *E*–*I*, distances over 200 nm were binned in the rightest column. (*F*–*L*) Histogram and cumulative distribution of Cav2.1–Munc13-1 distances for the 1st (*F*), the 2nd (*G*), the 3rd (*H*) and greater than or equal to the 4th (*I*) nearest Cav2.1 clusters relative to a given Munc13-1 cluster. Note that the 1st nearest Cav clusters corresponds to ones analyzed in Fig. 7. Statistical significance was tested with two samples Kolmogorov-Smirnov test for *C* (P = 0.09) and *E*–*I* (P = 0.57, P = 0.43, P = 0.99, P = 0.97, P = 0.32 respectively). (*J*–*L*) Cav2.1–Munc13-1 distances were averaged per animal and compared between control and forskolin for the 1st (*J*), the 2nd (*K*) and the 3rd nearest Cav2.1 clusters to the Munc13-1 cluster (*L*).

Supplementary Figure 10

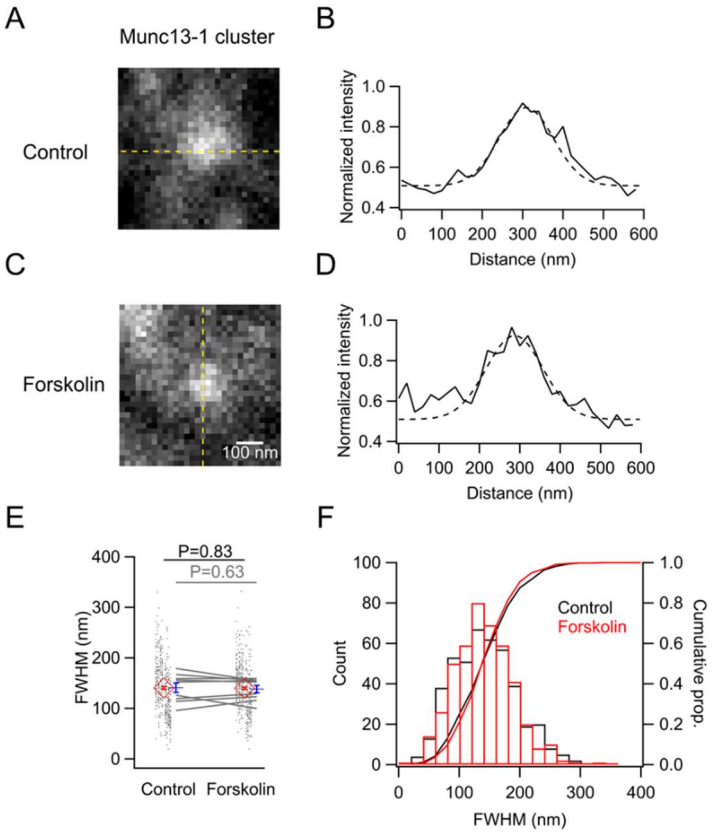

Supplementary Fig. 10. Forskolin application does not significantly alter the size of a given Munc13-1 cluster at hMFBs release sites.

(*A*–*D*) Cropped raw gSTED images representing Munc13-1 clusters near a given Cav2.1 cluster within the active zone in control (*A*) and forskolin-treated hippocampal slices (150 µm) (*C*). Intensities were measured at the yellow dotted lines in *A* and *C*, normalized to the peak intensity of the target cluster and plotted as solid lines in *B* and *D*. Intensity profiles across the sampling line were fitted to Gaussian function (dashed lines), and the full widths of half-maximum amplitude (FWHM) were estimated at 158.9 nm (*B*) and 155.5 nm (*D*) for these examples. (*E*) FWHMs in control (n = 440 synapses) and forskolin (n = 442 synapses). The values for the individual profiles (black dots) were vertically aligned animal by animal (9 animals), and their mean values per animal were compared (gray lines). The averages for these are shown as the red and blue symbols, respectively. (*F*) Histograms and cumulative proportions of FWHM in a 20-nm bin in control (black) and forskolin (red). Statistical significance was tested with two samples Kolmogorov-Smirnov test (P = 0.40).

References for Supporting Information

1. H. Kamiya, H. Shinozaki, C. Yamamoto, Activation of metabotropic glutamate receptor type 2/3 suppresses transmission at rat hippocampal mossy fibre synapses. *J. Physiol.* **493**, 447–455 (1996).

2. M. Frotscher et al., Fine structure of synapses on dendritic spines. *Front. Neuroanat*. **8**, 94 (2014).

3. I. Vida, M. Frotscher, A hippocampal interneuron associated with the mossy fiber system. *Proc. Natl. Acad. Sci.* **97**, 1275–1280 (2000).